The effects of solvent extraction on nanoporosity of marine-continental coal and mudstone

Yu Qi[1, 2], Yiwen Ju[1, *], Jianchao Cai[1,3], Yuan Gao[4], Hongjian Zhu[1], Cheng Hunag[1], Jianguang Wu[5], Shangzhi Meng[5], Wangang Chen[5]

1 Key Laboratory of Computational Geodynamics, College of Earth and Planetary Sciences, University of Chinese Academy of Sciences, Beijing 100049, China

2 Durham University, Department of Earth Sciences, Science Labs, Durham, DH1 3LE, UK

3 Hubei Subsurface Multi-scale Imaging Key Laboratory, Institute of Geophysics and Geomatics, China University of Geosciences, Wuhan 430074, China

4 Beijing Center for Physical & Chemical Analysis, Beijing 100089, China

5 China United Coalbed Methane Co Ltd, Beijing 100011, China

* **Corresponding author:** juyw03@163.com (Y. Ju).

Abstract

Coal and organic-rich mudstone develop massive nanopores, which control the storage of adsorbed and free gas, as well as fluid flows. Generation and retention of bitumen and hydrocarbons of oil window reservoirs add more uncertainty to the nanoporosity. Solvent extraction is a traditional way to regain unobstructed pore networks but may cause additional effects due to interactions with rocks, such as solvent adsorbing on clay surfaces or absorbing in kerogens. Selected marine-continental coal and mudstone in Eastern Ordos Basin were studied to investigate how pore structures are affected by these *in*-situ-sorptive compounds (namely residual bitumen and hydrocarbons) and altered by solvent extractions. Solvent extraction was performed to obtain bitumen-free subsamples. Organic petrology, bulk geochemical analyses and gas chromatography were used to characterize the samples and the extracts. Low pressure argon and carbon dioxide adsorptions were utilized to characterize the nanopore structures of the samples before and after extraction. The samples, both coal and mudstone, are in oil windows, with vitrinite reflectance ranging from 0.807 to 1.135 %. The coals are strongly affected by marine organic input, except for sample C-4; the mudstones are sourced by either marine or terrestrial organic input, or their mixture. As for the coals affected by marine organic input, residual

bitumen and hydrocarbons occupying or blocking pores < 10 nm becomes weak with thermal maturation. Bitumen derived from terrestrial organic matter mainly affects small pores, since coal asphaltene molecules are much smaller than petroleum asphaltene molecules. The mudstone M-2 with high extract production showed an increase of nanopores after extraction, due to the exposure of the filled or blocked pores. However, most transitional mudstones saw decreases of the pores because pore shrinkage caused by solvents adsorbing on and swelling clay minerals (mainly kaolinite and illite/smectite mixed layers) counteracts the released pore spaces. Solvent extractions on the coals significantly increased the micropores < 0.6 nm, since the heat of sorption of alkanes reaches the peak in the pores within 0.4-0.5 nm. By contrast, solvent extractions on the mudstones decreased the micropores ~ 0.35 nm, which is perhaps caused by evaporative drying of solvent displacing residual water in clay.

Key words

Coal; Mudstone; Marine-continental facies; Extraction; Bitumen; Nanopore

1 Introduction

Unconventional reservoirs are enriched with organic matter and share many characteristics of sealing units, including small pore size, low porosity and permeability [1, 2]. Pore networks of sediments in petroleum systems control the storage of adsorbed and free gas and fluid flows, which determine whether the sediments can be a reservoir or a cap rock. There have been studies on how pore structures are affected by lithology, mineralogy, total organic carbon (TOC), thermal maturity, fabric and diagenetic history [3-9], and how pore structures control the gas storage and migration [10-14]. Traditional and state-of-the-art experiments have been used to characterize porosity of fine-grained reservoirs.

Generation and retention of bitumen and hydrocarbon add more uncertainty to porosity of unconventional reservoirs in oil window. These *in*-situ-sorptive compounds (namely residual bitumen and hydrocarbons) condensed or adsorbed on the pores and thus change gas storage capacity [15].

Additionally, the alternation of porosity further changes the thermal and electrical conductivity, which have numerous applications in reservoir engineering and petrophysics [16-22]. Due to the abundance of bitumen, there is no correlation between microporosity and TOC in thermally immature shale [23, 24]. Solid-state nuclear magnetic resonance (NMR) and Fourier transform infrared spectroscopy (FTIR) were used to characterize the bulk chemical and structural information of bitumen and kerogen [25-27]. Synchrotron-based scanning transmission X-ray microscopy (STXM) combined with X-ray absorption near edge structure (XANES) spectra provides spatially-resolved geochemical information of bitumen and nanoporous pyrobitumen as a response to the thermal evolution of kerogen [28]. Residual bitumen infilling causes the absence of original organic pores, which has been verified by imaging unextracted and extracted mudstones [29, 30].

As for early mature or mature lacustrine shale, the residual bitumen in pores dramatically affects the pore structures and methane sorption [31]. Specific surface areas and pore volumes of marine and lacustrine shale generally increase after solvent extraction, apart from a few exceptions in marine shale [27, 31-34]. Bitumen-free porosity of shales after solvent extraction are higher than those measured in as-received samples, and bitumen-filled porosity decreases with thermal maturity [5]. All previous studies focused on oil prone mudstones (including lacustrine and marine mudstones), while transitional coal and mudstone were rarely reported. Compositions and textures of both organic matter and minerals of transitional sediments are much different from those of marine or lacustrine mudstones. For examples, transitional coal and mudstone may be sourced by a mixture of terrestrial and marine organic input. Additionally, high kaolinite content is a major feature of marine-continental or coal-bearing mudstone [35, 36].

Solvent extraction is suggested to be conducted to ensure that pore throats are unobstructed [32, 37]. However, chemical and physical interactions between solvent and kerogen or between solvent and minerals may alter the pore structure and cause inaccurate “real porosity” (porosity free of hydrocarbons and soluble bitumen). For examples, 1) Solvent extraction causes swelling of clay and kerogen; 2) solvent absorbs in organic matter and/or adsorbs on clay surfaces; 3) solvent extraction may completely or partially dissolve porous resins or asphaltenes [27, 32, 38].

This study aims to investigate how pore structures of marine-continental coal and mudstone are affected by *in*-situ-sorptive bitumen and hydrocarbons and altered by solvent extractions through comparing pore parameters of the samples before and after solvent extraction. Sample features, including thermal maturity, maceral compositions, hydrocarbons potential and TOC, were characterized by organic petrology, Rock-Eval pyrolysis and other bulk analysis methods. Gas chromatography was used to analyze the properties of the extracts. Nanopore structures were characterized by low pressure Argon (Ar) and carbon dioxide (CO_2) adsorption. This study clarifies what the extractable compounds of transitional coal and mudstone are like, and how they affect pore structures, and gains insights into the mechanisms of solvent extraction altering pore structures.

2 Samples and methods

2.1 Samples

Taiyuan and Shanxi Formations (belonging to Carboniferous and Permian Systems) in Ordos Basin, China were deposited in a marine-continental transitional facies. The transitional facies refers to the deposits between continental and marine settings, ranging from lagoon-tidal flat and fluvial-delta environments [39]. These strata are composed of a sequence of interbedded coal, mudstone and sandstone, forming a combination of different types of unconventional natural gas reservoirs. Joint development of coalbed methane, shale gas and tight gas has been proposed to raise recovery efficiency [39, 40].

This study focuses on the coal and mudstone in Taiyuan and Shanxi Formations, which are the weak links of the joint development. Samples were collected from collieries in Lin and Xing Counties, eastern Ordos Basin, and all belonged to the Taiyuan and Shanxi Formations. The coals are taken from the fresh coalfaces, and the mudstones, from the roofs or floors of the corresponding coal seams. The study bases on four coal and four mudstone samples. As mineralogy of transitional mudstone in the region is featured by high kaolinite content [33], two tonstein (nearly 100 percent of kaolinite) samples were included in the mudstone samples to amplify the effects of kaolinite. The mineral compositions of the selected four mudstones are shown in Tab. 1. The data were obtained by X-ray

diffractometry (XRD) following Chinese Industrial Standard SY/T 5163-2010. Mineral compositional analyses of bulk shale samples and their clay fractions were performed by a D/max-2005 X-ray diffractometer. XRD patterns were recorded from 2 to 45°(2θ) at the speed of 2°(2θ) per minute and the step width of 0.02°(2θ). M-1 and M-2 are tonstein samples, dominated by kaolinite. *in*-situ tonstein is a good material to study the role of kaolinite in mudstone. M-3 and M-4 contain a certain amount of quartz and clay minerals, and the clay minerals include illite/smectite mixed layers and kaolinite. Each sample (both coal and mudstone) was crushed to 40-60 mesh particles, some of which were further pulverized for total organic carbon analysis, Rock-Eval pyrolysis; the rest were split into two fractions. One fraction was kept as original samples, and the other was prepared for solvent extraction.

2.2 Methods

Thermal maturity was characterized by random vitrinite reflectance (R_o) of the coals. The coal samples were prepared for microscopic analysis by incident white light, following ASTM standard D2797. R_o was examined in incident white light at magnification of 500× oil immersion. Thermal maturity of the mudstones refers to the R_o of the corresponding coal samples, since they are collected from adjacent seams. Microscopic examination of kerogen was performed to evaluate maceral compositions. Coarse kerogen particles were obtained, following Chinese National Standard GB/T 19144, and the examination was performed by a transmitted light microscope equipped with ultraviolet (UV) light, following Chinese Industrial Standard SY/T 5125. Kerogen types were further calculated based on maceral compositions.

Total organic carbon (TOC) of the mudstones was measured with a Leco CS230 Carbon/Sulfur analyzer after the powered subsamples were soaked in heated hydrochloric acid solution to remove carbonates. The procedure followed Chinese National Standard GB/T 19145-2003. Rock-Eval pyrolysis was performed on 100-200 mesh mudstones. Related parameters were recorded. During the pyrolysis the first peak (S_1, mg HC/g rock) represents hydrocarbons distilled from rock. The second peak (S_2, mg HC/g rock) represents hydrocarbons generated by pyrolytic degradation. The third peak

(S_3, mg HC/g rock) represents milligrams of CO_2 generated from a gram of rock during temperature programming up to 390 °C. Temperature of maximum pyrolysis yield (T_{max}, °C) refers to the temperature at which the maximum amount of S_2 hydrocarbons is generated . Hydrogen index (HI, mg HC/g TOC) was calculated through dividing S_2 by TOC [41-43].

Solvent extraction was performed in a Soxhlet extractor with a solvent mixture of dichloromethane (DCM) and methanol (volume ratio 9:1). The samples were refluxed for more than 96 hours until the effluent distilled solvent was colourless and transparent. The extracts were evaporated to volatilize the solvent. The saturated fractions were separated from the extracts, and were then analyzed using gas chromatography (GC), flowing Chinese Industrial Standard SY/T 6196-1996. Saturated fraction separation and GC analysis were performed in the State Key Laboratory for Heavy Oil Processing, China.

Low-pressure argon (Ar) and carbon dioxide (CO_2) adsorptions were used to determine the nanopore structure of both original and extracted subsamples by a Autosorb iQ apparatus. The outgassing procedure prior to the adsorptions was conducted with a vacuum pumping system at 110 °C for 12 hours. It has been demonstrated that Ar at 87K and N_2 at 77K have excellent agreements in adsorption behaviors in mesopores [44]. The major difference between them is 1) Ar at 87 K fills micropores at a higher relative pressure, leading to accelerated equilibration and permits the measurement of high resolution adsorption isotherms; 2) Ar does not have a quadrupole moment as N_2. Ar adsorption at 87 K has been recommended to be an alternated method of nitrogen (N_2) adsorption at 77 K [45], because the bias caused by the orientation of a N_2 molecule may cause uncertainty in the value of molecular cross-sectional area – possibly ~ 20% for some surfaces [46]. CO_2 adsorption at 273 K provides more detailed information of micropores. Ar and CO_2 adsorptions have been combined to characterize nanopore structure of shale [47]. As for Ar adsorption, Brunauer−Emmett−Teller (BET) model was used to obtain specific surface areas (A_s), and Barrett, Joyner and Halenda (BJH) model was used to characterize pore size distributions (PSD). As for CO_2 adsorption, a density functional theory (DFT) model was chosen to calculate micropore specific surface areas ($A_{s\text{-}\mu}$) and micropore size distributions (PSD_μ).

3 Results

3.1 Sample features

Tab. 2 and 3 present thermal maturity and maceral compositions of the coal and mudstone samples. R_o of the coal samples ranges from 0.807 to 1.135 %, mainly in mid- to late- oil window. In this paper, we use "lower mature" to describe the maturity of the first two samples (R_o, 0.81 and 0.84 %) and "higher mature", the maturity of the last two samples (R_o, 1.01 and 1.14 %). For examples, the lower mature coals represent C-1 and C-2. Vitrinite is the major maceral composition of the coals, accounting for percentages of 61.63 -85.69 %, except for C-2. Vitrinite of C-2 takes up 29.94 %, and semivitrinite, 44.31 %. Thermal maturity of the mudstones refers to the corresponding coal samples. As for the mudstones, their macerals are much different between each other and are sourced by both terrestrial and aquatic-derived organic matter. Vitrinite and inertinite are associated with terrestrial organic matter while most sapropelinite and some liptinite are sourced from aquatic-derived organic matter. Total amount of vitrinite, inertinite and liptinite decreases with increasing distance to continent [48]. Maceral compositions were used for kerogen typing. Kerogen's type index (TI) varies from -76.5 to 94.5, and the kerogen types of the four mudstones can be categorized as III, I, III and II_1, respectively. Tab. 4 presents TOC and pyrolysis parameters of the mudstones. The TOC contents vary from 2.27 to 8.43 wt. % and M-2 accounts for the maximum value. T_{max} values range from 446.8 to 462.7 °C, and consist with the their R_o. S_2 values change from 0.82 to 9.35 mg HC/g rock and HI values range from 16.87 to 110.91 mg HC/ g rock, revealing different petroleum potentials. Three mudstones fall into the Type II region of the HI vs T_{max} plot, and one mudstone (M-2), Type III region (Fig. 1). The results of microscopic examination on kerogen and Rock-Eval pyrolysis do not completely agree with each other, due to their inadequate resolution [49], but both of them indicates the diversity of organic input.

3.3 Gas chromatography

The coals produce more extracts than the mudstones (0.25-4.02 g HC/ g rock for the coals and 0.040-

0.143 g HC/ g rock for the mudstones) (Tab. 5). The extract production of the coals is strongly affected by thermal maturity, while that of the mudstone increases with S_2 values (Fig. 2a and b). Gas chromatography provides information of normal alkanes (*n*-alkanes). *n*-alkane distributions of either the coals or the mudstones are diversiform (Fig. 3 and 4). *n*-alkanes can be divided into short-, mid- and long- chain (*n*-C_{15-20}, *n*-C_{21-25} and *n*-C_{26+}, respectively) [50]. The coals can be categorized to short-chain-*n*-alkane-dominated (*s*-dominated) and long-chain-*n*-alkane- dominated (*l*-dominated) coals. As for the coals, C-1, C-2 and C-3 are dominated by short-chain *n*-alkanes, with maximum peaks at *n*-C_{19}, *n*-C_{18} and *n*-C_{17} respectively. Their $\sum n\text{-}C_{21-}/\sum n\text{-}C_{22+}$ values range from 0.74 to 1.58. By contrast, C-4 mainly contains mid- and long-chain *n*-alkanes, with a maximum peak at *n*-C_{25} and a low $\sum n\text{-}C_{21-}/\sum n\text{-}C_{22+}$ value of 0.44. Pr/Ph is in the range of 0.95-2.48.

As for the mudstones, *n*-alkanes of M-1 and M-3 reach peaks at long-chain *n*-alkanes, while M-2 and M-3, short-chain *n*-alkanes. *n*-alkane distributions of M-1 and M-2 are unimodal, which indicates a single terrestrial organic input for *l*-dominated M-1 and a single marine organic input for *l*-dominated M-2. M-1 has the lowest $\sum n\text{-}C_{21-}/\sum n\text{-}C_{22+}$, 0.11; M-2 has the largest $\sum n\text{-}C_{21-}/\sum n\text{-}C_{22+}$, 2.36. *n*-alkane distributions of M-3 and M-4 are bimodal, with $\sum n\text{-}C_{21-}/\sum n\text{-}C_{22+}$ of 0.37 and 0.90 respectively, which indicates mixed organic input. M-3 is sourced by a lower percentage of marine organic input than M-4. The CPI of the coal samples (1.11-1.19) is larger than that of the mudstones (1.00-1.10), and the Pr/Ph of the coal samples (0.95-2.48, average 1.80) is also larger than that of the mudstones (0.76-1.35, average 1.11).

3.3 Low-pressure Ar adsorption

Tab. 6 presents the specific surface areas (A_s from Ar adsorption and $A_{s\text{-}\mu}$ from CO_2 adsorption) of the coal and mudstone samples. Fig. 5 and 6 show the PSD curves of the coals and mudstones, respectively. A_s of the original coals ranges from 0.42-1.97 m^2/g, average 0.88 m^2/g. Solvent extraction causes remarkable changes of pore structure in coals [26]. A_s of every coal sample increased after suffering solvent extraction, so did the PSD curves, and the changes of the lower mature coals are more remarkable (Fig. 5). Herein, we use “minor pores” and “larger pores” to

describe the pores in the left and right part of PSD curves, respectively. Minor pores of C-1 and C-4 increased much (Fig. 5a and d), and both minor and larger pores of C-2 increased after extraction (Fig. 5b). PSD curves of C-3 changed little (Fig. 5c).

A_s of the original mudstones is in the range of 1.64-10.93 m^2/g, average 6.84 m^2/g, much larger than that of the original coals, and does not change significantly after solvent extractions (Tab. 6). A_s and PSD curves of three mudstones (M-1, M-3 and M-4) dropped after solvent extraction (Tab. 6 and Fig. 6). Only M-2 saw a rise of A_s and PSD curve (Fig. 6b).

3.4 CO_2 adsorption

$A_{s\text{-}\mu}$ of the original coals is in the range of 57.15-89.04 m^2/g, much more than their A_s from Ar adsorption (0.42-1.97 m^2/g). Activated diffusion and kinetic restriction of nitrogen molecules at 77 K (or argon molecules at 87K) lead to low BET-A_s of coal [51, 52]. The $A_{s\text{-}\mu}$ decreases with thermal maturity, which agrees with previous conclusion that micropore volume of dry coal samples shows a minimum in the range of 1.2-1.4 % R_o [51]. $A_{s\text{-}\mu}$ of the coals generally increases after solvent extraction, especially for the lower mature coals (Fig.7a). $A_{s\text{-}\mu}$ of the mudstones ranges from 6.73 to 12.09 m^2/g. Comparing the $A_{s\text{-}\mu}$ of the coal and mudstone samples, it indicates that organic matter develops more micropores that minerals. $A_{s\text{-}\mu}$ of the two lower mature mudstones increased after solvent extraction, while the other two decreased (Fig. 7b). Micropore size distribution (PSD_μ) of the coals and mudstones are shown in Fig. 8 and Fig. 9. The PSD_μ curves of the coals generally have two peaks at ~ 0.6 nm and 0.8 nm, but those of the mudstones show an additional peak at 0.35 nm, which agrees with previous studies [53, 54]. The additional peak may be due to the clay minerals. After suffering solvent extraction, all the coal samples saw an increase of pores <0.6 nm, and the mudstone samples, an decrease of pores < 0.4 nm.

4 Discussion

4.1 Organic input and properties of extractable bitumen

Extract production of the coals decreases with thermal maturity, since asphaltenes and resins crack

soon after their formation or later [55]. Extract production of the mudstones is mainly controlled by S_2 (Fig 2b), rather than R_o. The inconformity of oil windows occurs between different types of kerogen, which weakens the effects of R_o to extract production. Oil window of type III kerogen (0.85-1.05% R_o to 1.5-2.0 % R_o) is much later than conventional oil window (0.5-0.5 % R_o to 1.3-1.35 R_o) [56-58]. Thus, the mixture of different types of organic matter does not has a regular oil-generation peak, and the extract production of mudstones shows no relationship with thermal maturity.

The Taiyuan and Shanxi Formations, a sequence of interbedded coal, mudstone and sandstone, deposited in a transitional environment, with alternating regression and transgression [39, 59]. Sedimentary environment affect not only clastic granularity, but also organic input and its preservation condition. Maceral analysis got the results that the coals are largely composed with vitrinite (or semivirtrinite for C-2) (Tab. 2). However, the *n*-alkane distribution patterns of three coals indicates strong influence of marine organic input. The disagreement is because microscopic analysis by incident light is not appropriate for examination of aquatic-derived organic matters [60]. *n*-alkane distribution patterns provide the information of organic precursors. Short-chain *n*-alkanes are considered to originate mostly from algae and microorganism, and mid- chain *n*-alkanes, aquatic plants and some moss species; long-chain *n*-alkanes are typical components of the epicuticular waxes of vascular plants [61-63]. *n*-alkanes can be altered by thermal and bacterial degradation [64]. Biodegradation is featured by losing *n*-alkanes and even acyclic isoprenoids [64], which does not occur in our samples. Thermal degradation generally cracks higher-molecular-weight *n*-alkanes to lighter products [64], while our higher mature samples (such as C-4 and M-3) have a high proportion of long-chain *n*-alkanes. Thus, the *n*-alkane distribution patterns of the samples were not remarkably altered by thermal or bacterial degradation and can reveal their precursors.

According to the *n*-alkane distribution patterns, the coals can be grouped into *s*-dominated and *l*-dominated coals. The first three coals (C-1, C-2 and C-3) are dominated by short-chain *n*-alkanes, which indicate the existence of marine organic matter. Pr/Ph ratio is an commonly used indicator of redox conditions and source of organic matter [65]. Coal samples, predominantly sourced from terrestrial plants, are expected to have Pr/Ph ratios > 3.0 (oxidizing conditions), while low values of

Pr/Pr ratio (<0.6) suggest anoxic conditions, and the ratios between 1.0-3.0 indicate intermediate conditions (subtoxic conditions) [64, 65]. Pr/Ph ratios of the first three coals are lower than the regressive line of the referenced coal samples [66, 67] (Fig. 10), which also supports the input of marine organic matter. Only C-4 has dominated by long-chain *n*-alkanes (Fig. 3d), supporting mainly terrestrial organic input. However, the *s*-dominated *n*-alkanes only indicate the existence of marine organic input, and do not evidence the three coals contain more marine organic input than terrestrial organic input. It is because conversion rates from kerogen to hydrocarbons differ in kerogen types (15-30 wt. % of terrestrial organic matter, 60 wt. % of marine organic matter with an HI of 600 mg HC/g TOC, 80 wt. % lacustrine organic matter with an HI of 800 mg HC/g TOC) [68]. Additionally, different preferential adsorption by kerogen of different compounds (polar compounds > aromatic hydrocarbons > saturated hydrocarbons) leads to differential expulsion or retention of selective compounds of bitumen and hydrocarbons [69-71].

Statistic data of kerogen's microscopic examination and the HI vs T_{max} plot support different kerogen types and a transitional sedimentary environment (Tab. 3 and Fig. 1). The diversity of *n*-alkane distributions of the mudstones is stronger than that of the coals. $\sum n\text{-}C_{21-}/\sum n\text{-}C_{22+}$ of the mudstones ranges from 0.11 to 2.36, and that of the coals, from 0.44 to 1.58. As for the mudstones, there is a relationship between HI and TI (Fig. 11a) and between $\sum n\text{-}C_{21-}/\sum n\text{-}C_{22+}$ and TI (Fig. 11b). It indicates that both HI and $\sum n\text{-}C_{21-}/\sum n\text{-}C_{22+}$ reveal the quality of organic matter in the mudstones. The *n*-alkane distribution patterns of the mudstones support aquatic-derived, terrigenous organic matter, or their mixture contribution. With $\sum n\text{-}C_{21-}/\sum n\text{-}C_{22+}$ increasing, the ratio of marine to terrestrial organic matter increases.

4.2 Pore changes by solvent extraction based on Ar adsorption

4.2.1 The effects on the coals

The coals contain much more extractable compounds than the mudstones. Removing the abundant extractable compounds causes great increases of specific surface areas and pore spaces. There is an uplift of PSD curves of every coal sample in either minor or larger pores, or entire ranges (Fig. 5).

Extract production determines the increments of pore volume, which partially affects A_s. Besides pore volume, A_s is also related to PSD, as small pores contribute more to A_s. Changes of PSD are controlled by the texture and location of extracts, which are affected by organic precursors and thermal maturity. Generally, there are watersheds between minor and larger pores on PSD curves around 10 nm. It has been reported that coal-bearing shale is rich in pores<10 nm [72]. The volumes of pores < 10 nm ($V_{<10\ nm}$) and within 10-50 nm ($V_{10\text{-}50\ nm}$), and their change rates after solvent extraction were calculated (Tab. 7). The *s*-dominated coals show an decreasing change rates of $V_{<10nm}$ with R_o increasing (Fig. 12a); the $V_{10\text{-}50\ nm}$ of the *s*-dominated coals is larger than the *l*-dominated coal (Fig. 12b). The change rates indicate the degree of pore filling by hydrocarbons and bitumen. The decreasing change rates of $V_{<10nm}$ of the *s*-dominated coals are caused by thermal maturation. At early stages of maturation, kerogen is decomposed to gas and bitumen. Some bitumen components including asphaltenes and resins also crack at the same time as or soon after their formation from kerogen [73]. Nanoporosity in organic matter begins to develop at R_o>0.6 to 0.9 % [74-76]. Removing the extractable bitumen and oil exposes porous kerogen and solid bitumen. With maturation, oil (mainly C_{6+} components) secondarily cracked to gas and carbon-rich residue such as solid bitumen is generated [55, 77, 78], and the bitumen contents decrease. Most residual hydrocarbons and some movable bitumen have been driven out to larger pores or fractures. And thus, removing the extractable parts of the high mature mudstones has a minimal effect on minor pores. Conclusively, marine organic input strongly affects the pore structure of the coals. The pores of lower mature coal are strongly blocked by bitumen and hydrocarbons, and thermal maturation weakens the blockage, especially for minor pores.

As coal asphaltenes are much smaller than petroleum asphaltenes [79, 80], C-4, which was mainly sourced by terrestrial organic input, has smaller asphaltene molecules. Thus, removing extractable compounds of C-4 mainly increases the minor pores, while all other coal samples see an increase of larger pores (Fig. 12b).

4.2.2 The effects on the mudstones

The change patterns of pore structures of the mudstones are totally different from those of the coals. A_s and PSD curves of three mudstones dropped after solvent extraction (Tab. 6 and Fig. 6), so did the $V_{<10nm}$ and $V_{10\text{-}50\ nm}$ (Fig 11). Previous studies generally found PSD curves of mudstone rise after solvent extraction, and the samples in their studies are dominantly lacustrine shale with moderate or relatively high TOC contents, and have high extract production [30, 33, 81]. Decreases of mesopore volumes or PSD curves of a few marine shales after solvent extraction have been reported [27, 32, 38]. While the PSD decreasing becomes more common for our samples. Only the M-2 shows an uplift of the PSD curve. The causes of the PSD changes include, on one hand, the extract productions of our samples are much lower than either lacustrine or marine shales, which means less pore space can be released by solvent extraction. Increments of pores caused by solvent extraction are remarkable for the high-extract samples, such as M-2. On the other hand, transitional mudstones contain rich kaolinite and other clay minerals [36], which swells by adsorbing solvent, causing the shrinkage of pores. Kaolinite contents of the mudstones range from 11.6 to 93.1 wt. %. PSD curves decrease when the negative effect of clay swelling is more remarkable than the positive effect of emptying extractable compounds in pores. M-1, M-3 and M-4 are in this case. Solvent extraction inducing swelling of montmorillonite and illite/smectite has been observed [38, 82]. The decrease of PSD of M-1, which is dominated by kaolinite (93.1 wt. %), demonstrates that kaolinite swells after interacting with solvent, and the effect can counteract the released pores in some cases. Interlayer surface of kaolinite can be chemically modified with methanol at room temperature [83]. Methoxy groups expand the interlayer space of kaolinite (the basal spacing of kaolinite and methanol-treated kaolinite are 0.72 and 0.86 nm, respectively) [83]. Hydrogen bonding solvents (such as methanol) swell clays more than polar aprotic and non-polar solvents [38], which means methanol causes stronger swelling of clay than original hydrocarbons. However, the positive effect of realizing pore spaces dominates over the negative effect of absorbing solvent if TOC is large enough, such as M2, with a TOC value of 8.43%.

Solvent swelling kerogen was also demonstrated [84, 85]. However, the negative effect of kerogen swelling is not as remarkable as the positive effect of emptying pores, since the pores of the coals and M-2 (samples with high TOC contents) increased after solvent extraction. Additionally, solvent extraction may also dissolve and extract porous resins or asphaltenes [38]. Adsorbate (Ar or CO_2) can dissolve in bitumen, which results in an overestimate of pore volumes of original samples [24, 27].

4.3 Micropore changes by solvent extraction based on CO_2 adsorption

Solvent extraction significantly increases the $A_{s\text{-}\mu}$ of the lower mature coals, but has very little effects on the higher mature coals. With maturation, extractable bitumen partly transforms to solid bitumen (pyrobitumen). Solubility of solid bitumen in solvents decreases with thermal maturity [86]. Thus, removing the extractable parts of high mature samples have a minimal effect on pore structures. From Fig. 8, all the coal samples see an increase of pores 0.3-0.6 nm, which contributes a lot to the increase of $A_{s\text{-}\mu}$. Only C-3 shows an decrease of $A_{s\text{-}\mu}$, due to the large decrease of pores within 0.6-0.9 nm. Preferential adsorption on the pores within 0.4-0.5 nm has been demonstrated by studying sorption of alkanes on zeolite. The heat of sorption as a function of mean pore diameter exhibits a maximum between 0.4 and 0.5 nm [87, 88]. At the pore sizes smaller than 0.5 nm repulsion forces start to be important [89]. Thus, solvent extractions mainly increase the pores 0.3- 0.6 nm.

The effects of solvent extraction on mudstone's pore structures also depend on the maturity. $A_{s\text{-}\mu}$ of the two lower mature mudstones increased after solvent extraction, while that of the two higher mature mudstones decreased (Fig. 7b). Thermal maturation changes the compositions and textures of bitumen, increasing the aromaticity and decreasing the H/C ratio of bitumen [90, 91]. Comparing with the coals, PSD_{μ} of the mudstones show an additional peak at 0.35 nm, which likely come from the clay minerals. Unlike the coal samples, the PSD_{μ} of the mudstones only saw decreases of the peak at ~ 0.35 nm (Fig. 9). Similar results (pores ~0.35 nm decreased after solvent extraction) were obtained by [81]. Solvent displacing residual water in micropores causes evaporative drying, which causes a reduction of porosity [92], or shrinks smaller pores (less than 0.6 nm) and enlarges larger pores [38, 93]. However, the evaporative drying is weak in porous organic matter. It is because that

kerogen is more likely hydrophobic, while inorganic part in mudstone is hydrophilic due to clay minerals [94, 95]. Gu et al. [96] indicates that OM porosity is water-accessible only for the pores > 20 nm. Thus, evaporative drying is weak in organic matterbut strong in inorganic parts of mudstones and causes reductions of clay micropores (~0.35 nm).

5 Conclusions

The flowing conclusions are obtained based on our limited samples and restricted to mid- to late-oil window marine-continental coal and mudstone.

(1) Thermal maturation decreases the extract amount of coal but do not affects mudstone significantly. *n*-alkane distribution indicates that the coals, except for C-4, are strongly influenced by marine organic input. Microscopic examination, Rock-Eval pyrolysis and *n*-alkane distribution patterns support the mudstones are soured by either marine or terrestrial organic input or their mixture.

(2) As for the short-chain-*n*-alkane-dominated coals, the effect of *in*-situ sorptive compounds occupying or blocking pores becomes weak with thermal maturation, due to the degradation of bitumen. The extractable compounds mainly affect the minor pores in long-chain- *n*-alkane-dominated C-4, since the molecules of coal asphaltene are much smaller than those of petroleum asphaltene.

(3) Differing from marine or lacustrine mudstone, nanopores of transitional mudstone generally decrease after suffering solvent extraction. Our mudstone samples show the kaolinite swelling caused by interacting with solvent has a strongly negative effect on pore sizes. As for the samples with high clay contents and low or moderate TOC contents, the effect of clay swelling can counteract or exceed the effect of releasing pore spaces. The sample with high TOC and high extract production is dominated by releasing occupied or blocked pores.

(4) Solvent extraction significantly increased the $A_{s\text{-}\mu}$ of the lower mature coals, but had little effect on the higher mature coals. Every coal sample saw an increase of the pores within 0.3-0.6 nm, since the heat of sorption of alkanes reaches the peak in the pores within 0.4-0.5 nm.

(5) Solvent extraction increased the $A_{s\text{-}\mu}$ of the lower mature mudstones but decreased the $A_{s\text{-}\mu}$ of the

higher mature mudstones. The micropores of the mudstones decreased at ~ 0.35 nm, which may due to the evaporative drying caused by solvent displacing residual water in micropores. Evaporative drying is weak in organic matter, but strong in clay minerals, since kerogen is more hydrophobic but minerals are hydrophilic.

(6) Due to the strong interactions between solvent and clay minerals, solvent extraction can not be used to obtain the "bitumen-free porosity" of transitional and other clay-rich mudstones.

Acknowledgements:

This research was financially supported by the National Natural Science Foundation of China (Grant Nos. 41530315, 41372213, 41572116), the National Science and Technology Major Project of China (Grant Nos. 2016ZX05066003, 2016ZX05066006), the Strategic Priority Research Program of the Chinese Academy of Sciences (Grant No. XDA05030100) and China Scholarship Council and British Council (Grant No. 201703780094). The authors also gratefully acknowledge Prof. Andrew C. Aplin from Durham University for his helpful comments on both structure and content of the paper.

References:

[1] Baruch ET, Kennedy MJ, Löhr SC, Dewhurst DN. Feldspar dissolution-enhanced porosity in Paleoproterozoic shale reservoir facies from the Barney Creek Formation (McArthur Basin, Australia). AAPG Bulletin 2015;99(09):1745-70.

[2] Aplin AC, Macquaker JHS. Mudstone diversity: Origin and implications for source, seal, and reservoir properties in petroleum systems. AAPG Bulletin 2011;95(12):2031-59.

[3] Rexer TF, Mathia EJ, Aplin AC, Thomas KM. High-Pressure Methane Adsorption and Characterization of Pores in Posidonia Shales and Isolated Kerogens. Energy & Fuels 2014;28(5):2886-901.

[4] Milliken KL, Curtis ME. Imaging pores in sedimentary rocks: Foundation of porosity prediction. Marine and Petroleum Geology 2016;73:590-608.

[5] Mathia EJ, Bowen L, Thomas KM, Aplin AC. Evolution of porosity and pore types in organic-rich, calcareous, Lower Toarcian Posidonia Shale. Marine and Petroleum Geology 2016;75:117-39.

[6] Loucks RG, Reed RM, Ruppel SC, Jarvie DM. Morphology, Genesis, and Distribution of Nanometer-Scale Pores in Siliceous Mudstones of the Mississippian Barnett Shale. Journal of Sedimentary Research 2009;79(12):848-61.

[7] Giffin S, Littke R, Klaver J, Urai JL. Application of BIB–SEM technology to characterize macropore morphology in coal. International Journal of Coal Geology 2013;114:85-95.

[8] Wang G, Ju Y, Yan Z, Li Q. Pore structure characteristics of coal-bearing shale using fluid invasion methods: A case study in the Huainan–Huaibei Coalfield in China. Marine and

Petroleum Geology 2015;62:1-13.
[9] Ju Y, Huang C, Sun Y, Wan Q, Lu X, Lu S, et al. Nanogeosciences: Research History, Current Status, and Development Trends. Journal of Nanoscience and Nanotechnology 2017;17(9):5930-65.
[10] Tan J, Horsfield B, Fink R, Krooss B, Schulz H-M, Rybacki E, et al. Shale Gas Potential of the Major Marine Shale Formations in the Upper Yangtze Platform, South China, Part III: Mineralogical, Lithofacial, Petrophysical, and Rock Mechanical Properties. Energy & Fuels 2014;28(4):2322-42.
[11] Tan J, Weniger P, Krooss B, Merkel A, Horsfield B, Zhang J, et al. Shale gas potential of the major marine shale formations in the Upper Yangtze Platform, South China, Part II: Methane sorption capacity. Fuel 2014;129:204-18.
[12] Qi Y, Ju Y, Jia T, Zhu H, Cai J. Nanoporous Structure and Gas Occurrence of Organic-Rich Shales. Journal of Nanoscience and Nanotechnology 2017;17(9):6942-50.
[13] Tan Y, Pan Z, Liu J, Wu Y, Haque A, Connell LD. Experimental study of permeability and its anisotropy for shale fracture supported with proppant. Journal of Natural Gas Science and Engineering 2017;44:250-64.
[14] Yuan W, Pan Z, Li X, Yang Y, Zhao C, Connell LD, et al. Experimental study and modelling of methane adsorption and diffusion in shale. Fuel 2014;117:509-19.
[15] Li J, Lu S, Xie L, Zhang J, Xue H, Zhang P, et al. Modeling of hydrocarbon adsorption on continental oil shale: A case study on n -alkane. Fuel 2017;206:603-13.
[16] Wei W, Cai J, Hu X, Han Q. An electrical conductivity model for fractal porous media. Geophysical Research Letters 2015;42(12):4833-40.
[17] Wei W, Cai J, Hu X, Han Q, Liu S, Zhou Y. Fractal analysis of the effect of particle aggregation distribution on thermal conductivity of nanofluids. Physics Letters A 2016;380(37):2953-6.
[18] Cai J, Hu X, Xiao B, Zhou Y, Wei W. Recent developments on fractal-based approaches to nanofluids and nanoparticle aggregation. International Journal of Heat and Mass Transfer 2017;105:623-37.
[19] Cai J, Wei W, Hu X, Wood DA. Electrical conductivity models in saturated porous media: A review. Earth-Science Reviews 2017;171:419-33.
[20] Li J, Zhang P, Lu S, Xue H, Zhang P, Ma F. Microstructural characterization of the clay-rich oil shales by nuclear magnetic resonance (NMR). Journal of Nanoscience and Nanotechnology 2017;17(9):7026-34.
[21] Lyu Q, Long X, Ranjith PG, Tan J, Kang Y, Wang Z. Experimental investigation on the mechanical properties of a low-clay shale with different adsorption times in sub-/super-critical CO 2. Energy 2018;147:1288-98.
[22] Lyu Q, Long X, Ranjith PG, Tan J, Kang Y. Experimental investigation on the mechanical behaviours of a low-clay shale under water-based fluids. Engineering Geology 2018;233:124-38.
[23] Furmann A, Mastalerz M, Bish D, Schimmelmann A, Pedersen PK. Porosity and pore size distribution in mudrocks from the Belle Fourche and Second White Specks Formations in Alberta, Canada. AAPG Bulletin 2016;100(08):1265-88.
[24] Ross DJK, Bustin RM. The importance of shale composition and pore structure upon gas storage potential of shale gas reservoirs. Marine and Petroleum Geology 2009;26(6):916-27.
[25] Suzuki T, Itoh M, Takegami Y, Watanabe Y. Chemical structure of tar-sand bitumens by 13C and 1H n.m.r. spectroscopic methods. Fuel 1982;61(5):402-10.
[26] Furmann A, Mastalerz M, Brassell SC, Schimmelmann A, Picardal F. Extractability of biomarkers from high- and low-vitrinite coals and its effect on the porosity of coal. International Journal of Coal Geology 2013;107:141-51.
[27] Wei L, Mastalerz M, Schimmelmann A, Chen Y. Influence of Soxhlet-extractable bitumen and oil on porosity in thermally maturing organic-rich shales. International Journal of Coal Geology 2014;132:38-50.
[28] Bernard S, Wirth R, Schreiber A, Schulz H-M, Horsfield B. Formation of nanoporous pyrobitumen residues during maturation of the Barnett Shale (Fort Worth Basin). International

Journal of Coal Geology 2012;103:3-11.
[29] Löhr SC, Baruch ET, Hall PA, Kennedy MJ. Is organic pore development in gas shales influenced by the primary porosity and structure of thermally immature organic matter? Organic Geochemistry 2015;87:119-32.
[30] Li J, Zhou S, Li Y, Ma Y, Yang Y, Li C. Effect of organic matter on pore structure of mature lacustrine organic-rich shale: A case study of the Triassic Yanchang shale, Ordos Basin, China. Fuel 2016;185:421-31.
[31] Guo H, Jia W, Peng Pa, Lei Y, Luo X, Cheng M, et al. The composition and its impact on the methane sorption of lacustrine shales from the Upper Triassic Yanchang Formation, Ordos Basin, China. Marine and Petroleum Geology 2014;57:509-20.
[32] Zargari S, Canter KL, Prasad M. Porosity evolution in oil-prone source rocks. Fuel 2015;153:110-7.
[33] Xiong F, Jiang Z, Chen J, Wang X, Huang Z, Liu G, et al. The role of the residual bitumen in the gas storage capacity of mature lacustrine shale: A case study of the Triassic Yanchang shale, Ordos Basin, China. Marine and Petroleum Geology 2016;69:205-15.
[34] Valenza JJ, Drenzek N, Marques F, Pagels M, Mastalerz M. Geochemical controls on shale microstructure. Geology 2013;41(5):611-4.
[35] Xiong F, Jiang Z, Li P, Wang X, Bi H, Li Y, et al. Pore structure of transitional shales in the Ordos Basin, NW China: Effects of composition on gas storage capacity. Fuel 2017;206:504-15.
[36] Dill HG. Kaolin: Soil, rock and ore From the mineral to the magmatic, sedimentary and metamorphic environments. Earth-Science Reviews 2016;161:16-129.
[37] Lasswell PM. Shale routine & special core analysis. Weatherford Laboratories; 2011.
[38] DiStefano VH, McFarlane J, Anovitz LM, Stack AG, Gordon AD, Littrell KC, et al. Extraction of organic compounds from representative shales and the effect on porosity. Journal of Natural Gas Science and Engineering 2016;35:646-60.
[39] Li Y, Tang D, Wu P, Niu X, Wang K, Qiao P, et al. Continuous unconventional natural gas accumulations of Carboniferous-Permian coal-bearing strata in the Linxing area, northeastern Ordos basin, China. Journal of Natural Gas Science and Engineering 2016;36:314-27.
[40] Ju Y, Wang G, Bu H, Li Q, Yan Z. China organic-rich shale geologic features and special shale gas production issues. Journal of Rock Mechanics and Geotechnical Engineering 2014;6(3):196-207.
[41] Peters KE. Guidelines for Evaluating Petroleum Source Rock Using Programmed Pyrolysis. AAPG Bulletin 1986;70(3):318-29.
[42] Espitalié J, Laporte JL, Madec M, Marquis F, Leplat P, Paulet J, et al. Méthode rapide de caractérisation des roches mètres, de leur potentiel pétrolier et de leur degré d'évolution. Revue de l'Institut français du Pétrole 1977;32(1):23-42.
[43] P. Tissot B, H. Welte D. Petroleum formation and occurrence. Springer-Verlag Berlin Heidelberg; 1984.
[44] Thommes M, Smarsly B, Groenewolt M, Ravikovitch PI, Neimark AV. Adsorption hysteresis of nitrogen and argon in pore networks and characterization of novel micro- and mesoporous silicas. Langmuir 2006;22(2):756-64.
[45] Thommes M, Kaneko K, Neimark AV, Olivier JP, Rodriguez-Reinoso F, Rouquerol J, et al. Physisorption of gases, with special reference to the evaluation of surface area and pore size distribution (IUPAC Technical Report). Pure and Applied Chemistry 2015;87(9-10): 1051–69.
[46] Rouquerol J, Rouquerol F, Llewellyn P, Maurin G, Sing KSW. Adsorption by Powders and Porous Solids: Principles, Methodology and Applications. Oxford: Academic Press; 2014.
[47] Zhang L, Xiong Y, Li Y, Wei M, Jiang W, Lei R, et al. DFT modeling of CO 2 and Ar low-pressure adsorption for accurate nanopore structure characterization in organic-rich shales. Fuel 2017;204:1-11.
[48] Boucsein B, Stein R. Black shale formation in the late Paleocene/early Eocene Arctic Ocean and paleoenvironmental conditions: New results from a detailed organic petrological study.

Marine and Petroleum Geology 2009;26(3):416-26.
[49] Larter SR, Senftle JT. Improved kerogen typing for petroleum source rock analysis. Nature 1985;318:277.
[50] Zdravkov A, Bechtel A, Sachsenhofer RF, Kortenski J. Palaeoenvironmental implications of coal formation in Dobrudzha Basin, Bulgaria: Insights from organic petrological and geochemical properties. International Journal of Coal Geology 2017;180:1-17.
[51] Prinz D, Littke R. Development of the micro- and ultramicroporous structure of coals with rank as deduced from the accessibility to water. Fuel 2005;84(12-13):1645-52.
[52] Mahajan OP. Co2 Surface-Area of Coals - the 25-Year Paradox. Carbon 1991;29(6):735-42.
[53] Prinz D, Pyckhout-Hintzen W, Littke R. Development of the meso- and macroporous structure of coals with rank as analysed with small angle neutron scattering and adsorption experiments. Fuel 2004;83(4-5):547-56.
[54] Yang R, He S, Hu Q, Hu D, Zhang S, Yi J. Pore characterization and methane sorption capacity of over-mature organic-rich Wufeng and Longmaxi shales in the southeast Sichuan Basin, China. Marine and Petroleum Geology 2016;77:247-61.
[55] Bernard S, Horsfield B. Thermal Maturation of Gas Shale Systems. Annual Review of Earth and Planetary Sciences 2014;42(1):635-51.
[56] Petersen HI. The petroleum generation potential and effective oil window of humic coals related to coal composition and age. International Journal of Coal Geology 2006;67(4):221-48.
[57] Behar F, Vandenbroucke M, Tang Y, Marquis F, Espitalie J. Thermal cracking of kerogen in open and closed systems: Determination of kinetic parameters and stoichiometric coefficients for oil and gas generation. Organic Geochemistry 1997;26(5-6):321-39.
[58] Tissot BP, Pelet R, Ungerer P. Thermal History of Sedimentary Basins, Maturation Indexes, and Kinetics of Oil and Gas Generation. Aapg Bull 1987;71(12):1445-66.
[59] Xu H, Cao D, Li Y, Liu J, Niu X, Zhang Y, et al. Geochemical and Preliminary Reservoir Characteristics of the Carboniferous–Permian Coal-Bearing Strata in the Junger Area, Northeastern Ordos Basin, China: Source Implications for Unconventional Gas. Energy and Fuels 2016;30(9):6947-57.
[60] Scott AC. Coal petrology and the origin of coal macerals: a way ahead? International Journal of Coal Geology 2002;50(1-4):119-34.
[61] Cranwell PA. Organic geochemistry of Cam Loch (Sutherland) sediments. Chemical Geology 1977;20:205-21.
[62] Ficken KJ, Li B, Swain DL, Eglinton G. An n-alkane proxy for the sedimentary input of submerged/floating freshwater aquatic macrophytes. Organic Geochemistry 2000;31(7-8):745-9.
[63] Eglinton G, Hamilton RJ. Leaf Epicuticular Waxes. Science 1967;156(3780):1322-35.
[64] Peters KE, Peters KE, Walters CC, Moldowan J. The biomarker guide. Cambridge university press; 2005.
[65] Peters KE, Moldowan JM. The biomarker guide: interpreting molecular fossils in petroleum and ancient sediments. Prentice Hall, Englewood Cliffs, NJ; 1993.
[66] Jasper K, Hartkopf-Fröder C, Flajs G, Littke R. Evolution of Pennsylvanian (Late Carboniferous) peat swamps of the Ruhr Basin, Germany: Comparison of palynological, coal petrographical and organic geochemical data. International Journal of Coal Geology 2010;83(4):346-65.
[67] Böcker J, Littke R, Hartkopf-Fröder C, Jasper K, Schwarzbauer J. Organic geochemistry of Duckmantian (Pennsylvanian) coals from the Ruhr Basin, western Germany. International Journal of Coal Geology 2013;107:112-26.
[68] Espitalié J, Deroo G, Marquis F. La pyrolyse Rock-Eval et ses applications. Revue de l'Institut français du Pétrole 1985;40(5):563-79.
[69] Littke R, Leythaeuser D, Radke M, Schaefer RG. Petroleum Generation and Migration in Coal Seams of the Carboniferous Ruhr Basin, Northwest Germany. Organic Geochemistry 1990;16(1-3):247-58.

[70] Ritter U. Solubility of petroleum compounds in kerogen. Organic Geochemistry 2003;34(3):319-26.
[71] Sandvik EI, Young WA, Curry DJ. Expulsion from Hydrocarbon Sources - the Role of Organic Absorption. Organic Geochemistry 1992;19(1-3):77-87.
[72] Pan J, Peng C, Wan X, Zheng D, Lv R, Wang K. Pore structure characteristics of coal-bearing organic shale in Yuzhou coalfield, China using low pressure N 2 adsorption and FESEM methods. Journal of Petroleum Science and Engineering 2017;153:234-43.
[73] Behar F, Roy S, Jarvie D. Artificial maturation of a Type I kerogen in closed system: Mass balance and kinetic modelling. Organic Geochemistry 2010;41(11):1235-47.
[74] Curtis ME, Cardott BJ, Sondergeld CH, Rai CS. Development of organic porosity in the Woodford Shale with increasing thermal maturity. International Journal of Coal Geology 2012;103:26-31.
[75] Loucks RG, Reed RM, Ruppel SC, Hammes U. Spectrum of pore types and networks in mudrocks and a descriptive classification for matrix-related mudrock pores. AAPG Bulletin 2012;96(6):1071-98.
[76] Cardott BJ, Landis CR, Curtis ME. Post-oil solid bitumen network in the Woodford Shale, USA — A potential primary migration pathway. International Journal of Coal Geology 2015;139:106-13.
[77] Jarvie DM, Hill RJ, Ruble TE, Pollastro RM. Unconventional shale-gas systems: The Mississippian Barnett Shale of north-central Texas as one model for thermogenic shale-gas assessment. AAPG Bulletin 2007;91(4):475-99.
[78] Lewan MD, Winters JC, Mcdonald JH. Generation of oil-like pyrolyzates from organic-rich shales. Science 1979;203(4383):897-9.
[79] Badre S, Carla Goncalves C, Norinaga K, Gustavson G, Mullins OC. Molecular size and weight of asphaltene and asphaltene solubility fractions from coals, crude oils and bitumen. Fuel 2006;85(1):1-11.
[80] Groenzin H, Mullins OC. Molecular size and structure of asphaltenes from various sources. Energy & Fuels 2000;14(3):677-84.
[81] Yu Y, Luo X, Cheng M, Lei Y, Wang X, Zhang L, et al. Study on the distribution of extractable organic matter in pores of lacustrine shale: An example of Zhangjiatan Shale from the Upper Triassic Yanchang Formation, Ordos Basin, China. Interpretation 2017;5(2):SF109-SF26.
[82] Geramian M, Osacky M, Ivey DG, Liu Q, Etsell TH. Effect of Swelling Clay Minerals (Montmorillonite and Illite-Smectite) on Nonaqueous Bitumen Extraction from Alberta Oil Sands. Energy & Fuels 2016.
[83] Komori Y, Enoto H, Takenawa R, Hayashi S, Sugahara Y, Kuroda K. Modification of the interlayer surface of kaolinite with methoxy groups. Langmuir 2000;16(12):5506-8.
[84] Larsen JW, Li S. Solvent Swelling Studies of Green River Kerogen. Energy and Fuels 1994;8(4):932-6.
[85] Ertas D, Kelemen SR, Halsey TC. Petroleum expulsion Part 1. Theory of kerogen swelling in multicomponent solvents. Energy and Fuels 2006;20(1):295-300.
[86] Hwang RJ, Teerman SC, Carlson RM. Geochemical comparison of reservoir solid bitumens with diverse origins. Organic Geochemistry 1998;29(1-3):505-17.
[87] Bates SP, vanWell WJM, vanSanten RA, Smit B. Energetics of n-alkanes in zeolites: A configurational-bias Monte Carlo investigation into pore size dependence. Journal of the American Chemical Society 1996;118(28):6753-9.
[88] Gribov EN, Sastre G, Corma A. Influence of pore dimension and sorption configuration on the heat of sorption of hexane on monodimensional siliceous zeolites. J Phys Chem B 2005;109(50):23794-803.
[89] Eder F, Lercher JA. On the role of the pore size and tortuosity for sorption of alkanes in molecular sieves. J Phys Chem B 1997;101(8):1273-8.

[90] Craddock PR, Le Doan TV, Bake K, Polyakov M, Charsky AM, Pomerantz AE. Evolution of Kerogen and Bitumen during Thermal Maturation via Semi-Open Pyrolysis Investigated by Infrared Spectroscopy. Energy & Fuels 2015;29(4):2197-210.
[91] Pomerantz AE, Le Doan TV, Craddock PR, Bake KD, Kleinberg RL, Burnham AK, et al. Impact of Laboratory-Induced Thermal Maturity on Asphaltene Molecular Structure. Energy & Fuels 2016;30(9):7025-36.
[92] Thompson ML, Mcbride JF, Horton R. Effects of Drying Treatments on Porosity of Soil Materials. Soil Sci Soc Am J 1985;49(6):1360-4.
[93] Job N, Théry A, Pirard R, Marien J, Kocon L, Rouzaud J-N, et al. Carbon aerogels, cryogels and xerogels: Influence of the drying method on the textural properties of porous carbon materials. Carbon 2005;43(12):2481-94.
[94] Mitchell A, Hazell L, Webb K. Wettability determination: pore surface analysis. *SPE Annual Technical Conference and Exhibition.* Society of Petroleum Engineers; 1990.
[95] Odusina EO, Sondergeld CH, Rai CS. NMR Study of Shale Wettability. *Canadian Unconventional Resources Conference.* Calgary, Alberta, Canada: Society of Petroleum Engineers; 2011.
[96] Gu X, Mildner DFR, Cole DR, Rother G, Slingerland R, Brantley SL. Quantification of Organic Porosity and Water Accessibility in Marcellus Shale Using Neutron Scattering. Energy & Fuels 2016;30(6):4438-49.

Table 1 Mineral composition of the mudstone samples.

Sample	Quartz (wt. %)	Feldspar (wt. %)	Pyrite (wt. %)	Smectite (wt. %)	Illite- Smectite mixed layer (wt. %)	Illite (wt. %)	Kaolinite (wt. %)	Chlorite (wt. %)
M-1	/	/	5.1	/	/	0.9	93.1	0.9
M-2	1.2	/	0.5	2.0	/	3.9	91.4	1.0
M-3	46.1	6.0	/	/	26.3	6.2	11.6	3.8
M-4	34.6	1.0	/	/	14.2	3.2	44.4	2.6

Table 2 Vitrinite reflectance and maceral composition of the coal samples.

Sample	R_o(%)	Maceral composition (v/v %)							
		Vitrtrinite	Semivirtrinite	Fusinite	Semifusinite	Liptinite	Clay	Carbonatite	Pyrite
C-1	0.81	61.63	3.58	21.07	4.38	2.98	2.78	3.58	/
C-2	0.84	29.94	44.31	0.20	10.58	2.40	10.18	2.40	/
C-3	1.01	85.69	0.19	1.74	1.74	3.48	7.16	/	/
C-4	1.14	80.78	7.06	2.55	6.08	1.18	1.77	0.59	/

Table 3 Maceral compositions of the mudstone samples.

Sample	Maceral composition (v/v %)					TI[a]	Kerogen Types[b]
	Sapropelinite	Resinite	Liptinite without Resinite	Vitrinite	Inertinite		
M-1	/	/	4	70	26	-76.5	III
M-2	89	/	11	/	/	94.5	I
M-3	2	/	10	74	14	-62.5	III
M-4	44	/	48	6	2	61.5	II_1

[a] Kerogen type index (TI) is calculated by the following equation, $TI=100a+80b_1+50b_2+(-75)c+(-100)d$, where a, b_1, b_2, c and d are the percentage of sapropelinite, resinite, liptinite free of resinite, vitrinite and inertinite, respectively, %.

[b] Kerogen types is determined by TI. The ranges of TI values of type I and II_1, type II_1 and II_2, and type II_2 and III, are >80, 80-40, 40-0 and <0, respectively.

Table 4 TOC and Rock-Eval pyrolysis parameters of the mudstone samples

Sample	TOC（wt. %）	T_{max} (℃)	S_1 (mg HC/g rock)	S_2 (mg HC/g rock)	HI (mg HC/g TOC)
M-1	4.86	446.8	0.22	0.82	16.87
M-2	8.43	447.7	0.48	9.35	110.91
M-3	2.27	461.4	0.36	1.58	69.60
M-4	4.7	462.7	0.53	4.73	100.64

Table 5 Extract production and organic geochemical parameters from gas chromatography

Samples	Extract production (g HC/ g rock)	Max-peak	C_{21-}/C_{22+}	n-C_{17}/n-C_{31}	Pr/Ph	Pr/n-C_{17}	Ph/n-C_{18}	CPI
C-1	4.02	n-C_{19}	0.74	2.77	2.12	0.92	0.45	1.11
C-2	2.70	n-C_{18}	1.58	7.34	2.48	0.29	0.11	1.13
C-3	0.36	n-C_{17}	1.11	5.70	1.63	0.63	0.39	1.17
C-4	0.25	n-C_{25}	0.44	1.55	0.95	0.17	0.15	1.19
M-1	0.05	n-C_{27}	0.11	0.23	0.76	0.88	0.82	1.07
M-2	0.14	n-C_{16}	2.36	9.45	1.35	0.44	0.35	1.10
M-3	0.04	n-C_{26}	0.37	1.12	1.22	0.65	0.44	1.05
M-4	0.07	n-C_{18}	0.90	2.66	1.1	0.55	0.47	1.00

Table 6 Parameters of pore structure before and after solvent extraction. A_s represents specific surface area obtained by low-pressure Ar adsorption and $A_{s\text{-}\mu}$ represents micropore specific surface area obtained by low pressure CO_2 adsorption.

Sample	A_s (m^2/g)		$A_{s\text{-}\mu}$ (m^2/g)	
	Original	Extracted	Original	Extracted
C-1	0.42	1.41	89.04	128.11
C-2	1.97	3.5	72.88	111.45
C-3	0.77	0.82	61.93	60.77
C-4	0.34	0.52	57.15	61.53
M-1	1.64	1.18	6.73	11.49
M-2	7.61	8.56	12.09	12.59
M-3	7.16	5.96	9.23	7.72
M-4	10.93	7.28	11.85	11.58

Table 7 Changes of the minor and larger pores caused by solvent extraction. The results were obtained from low-pressure Ar adsorption.

Sample	Pores<10nm			Pores between 10-50nm ($10^{-3}m^2$/g)		
	Original ($10^{-3}m^2$/g)	Extracted ($10^{-3}m^2$/g)	Change Rate (%)	Original ($10^{-3}m^2$/g)	Extracted ($10^{-3}m^2$/g)	Change Rate (%)
C-1	0.40	1.36	243	1.75	3.67	71
C-2	1.88	2.74	46	7.72	13.73	88
C-3	0.72	0.75	4	1.33	1.68	53
C-4	0.32	0.44	36	0.87	1.01	5
M-1	1.42	0.94	-34	6.64	5.69	-9
M-2	7.20	7.89	10	11.77	13.91	32
M-3	5.54	5.41	-2	17.47	13.26	-34
M-4	8.45	6.86	-19	17.83	13.33	-31

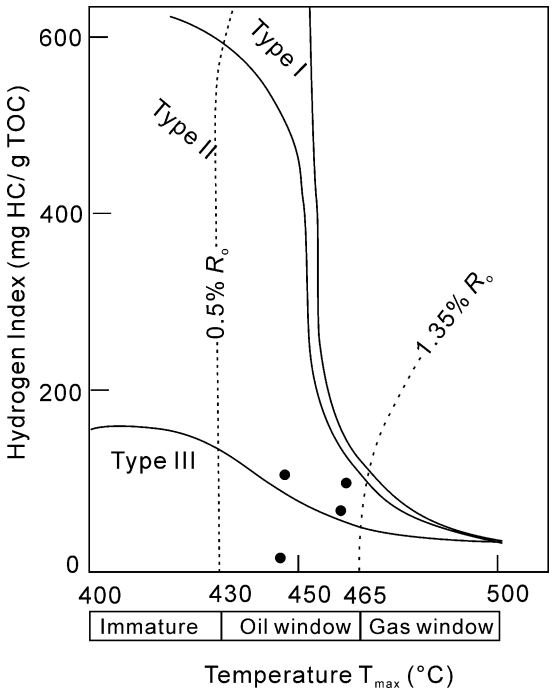

Figure 1 HI vs T_{max} plot of the mudstone samples.

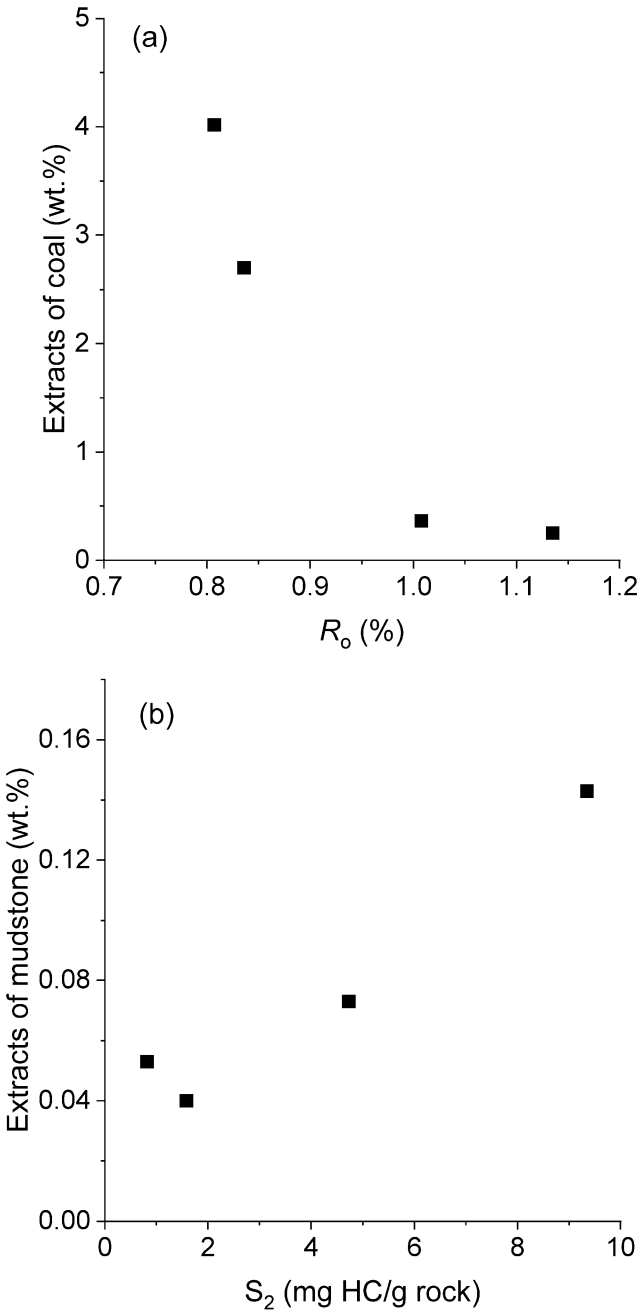

Figure 2 (a) Extract production of the coals decreases with vitrinite reflectance; b) Extract production of the mudstones increases with S_2 values.

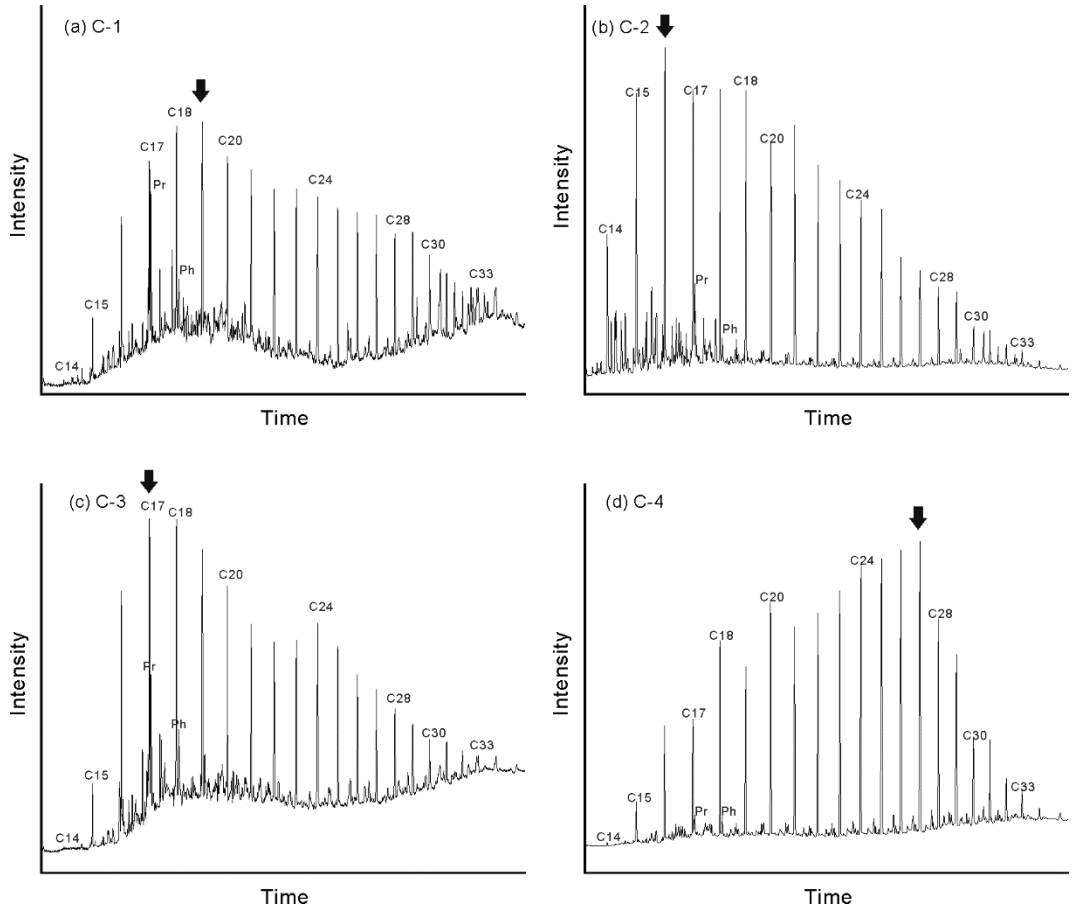

Figure 3 *n*-alkane distribution of the coal samples. Black arrows are primary peaks of each sample.

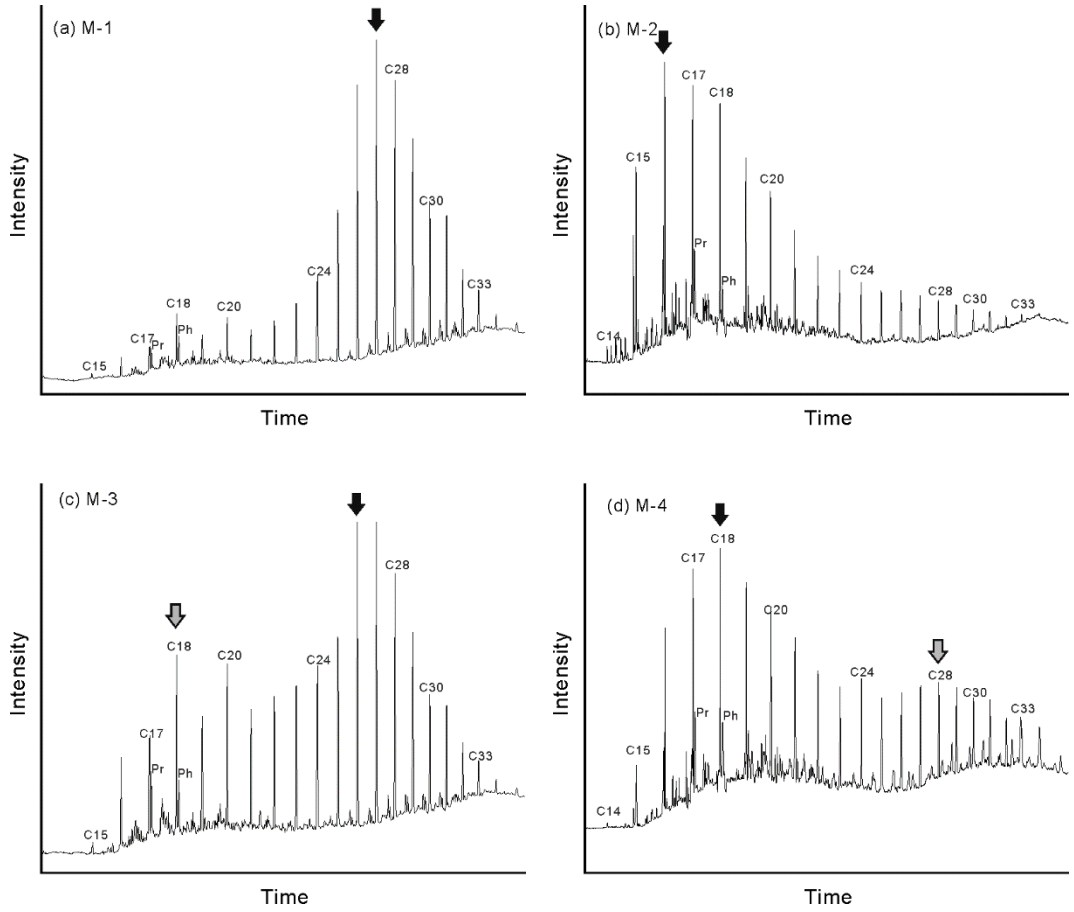

Figure 4 *n*-alkane distribution of shale samples (Black arrows are primary peaks, and grey arrows are secondary peaks)

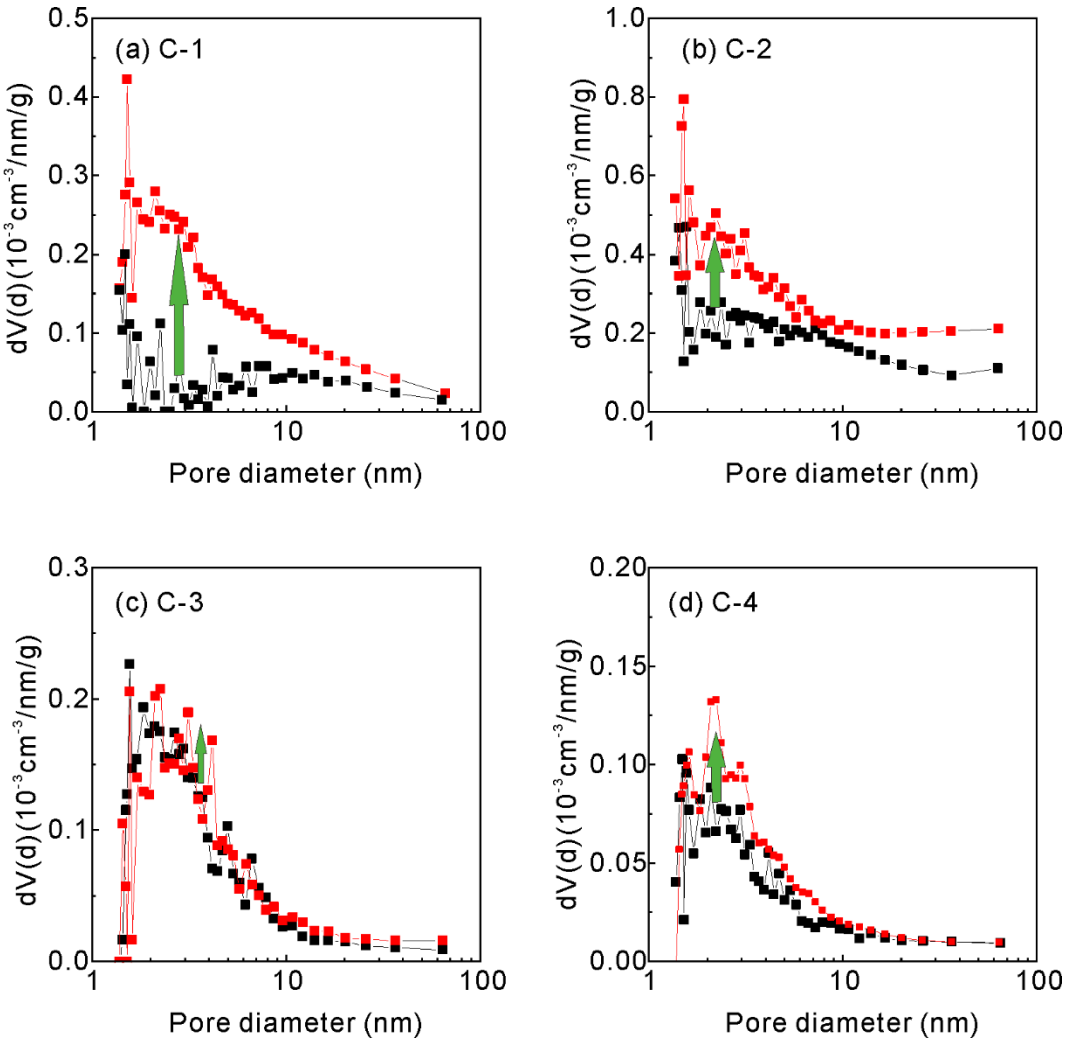

Figure 5 Pore size distribution curves (Ar adsorptions) of the coal samples. Black symbols and lines represent the original coals, and red symbols and lines, the extracted coals. The arrows indicate the increase of PSD curves after extraction. [print in colour]

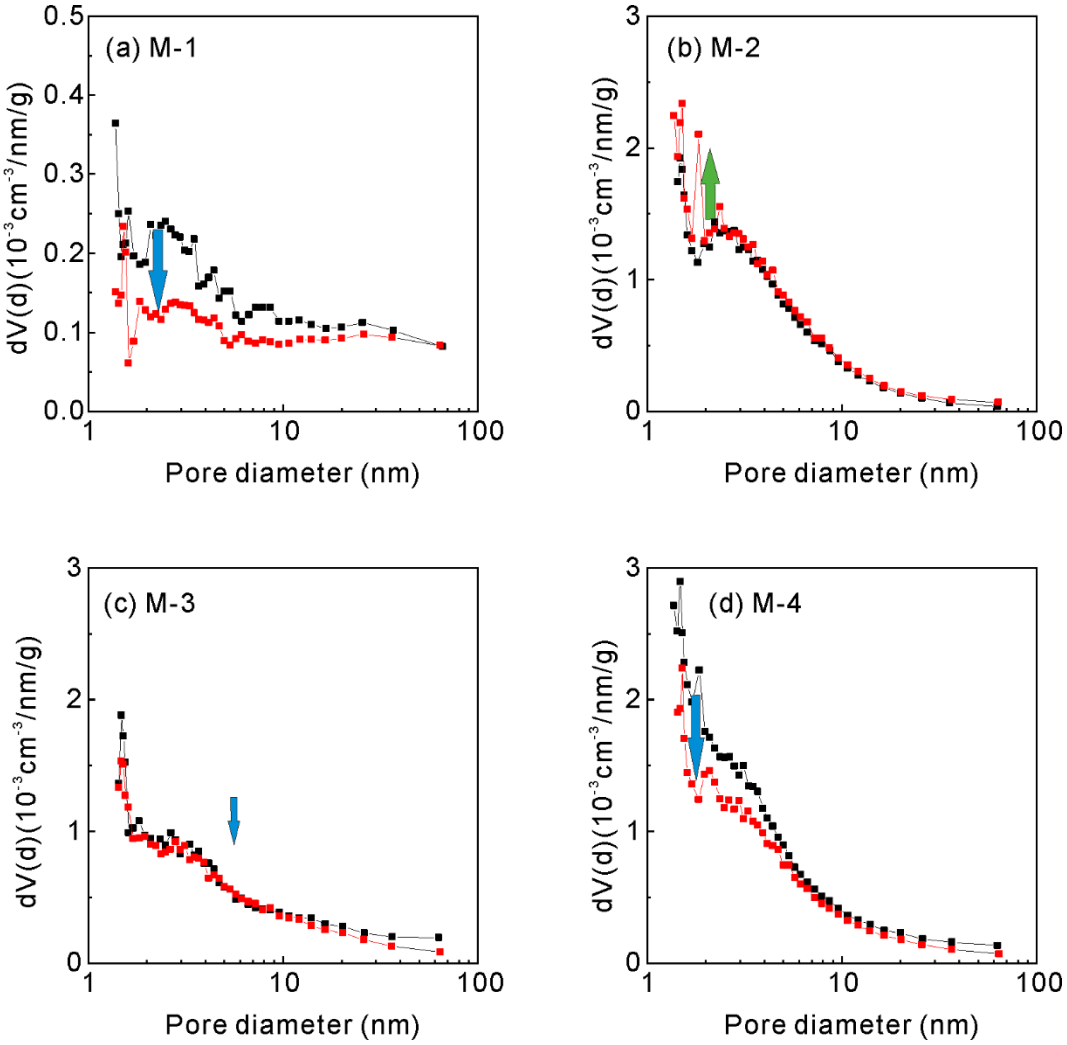

Figure 6 Pore size distribution curves (Ar adsorptions) of the mudstone samples Black symbols and lines represent the original mudstones, and red symbols and lines, the extracted mudstones. The blue and green arrows indicate the increase and decline of PSD curves after extraction, respectively. [print in colour]

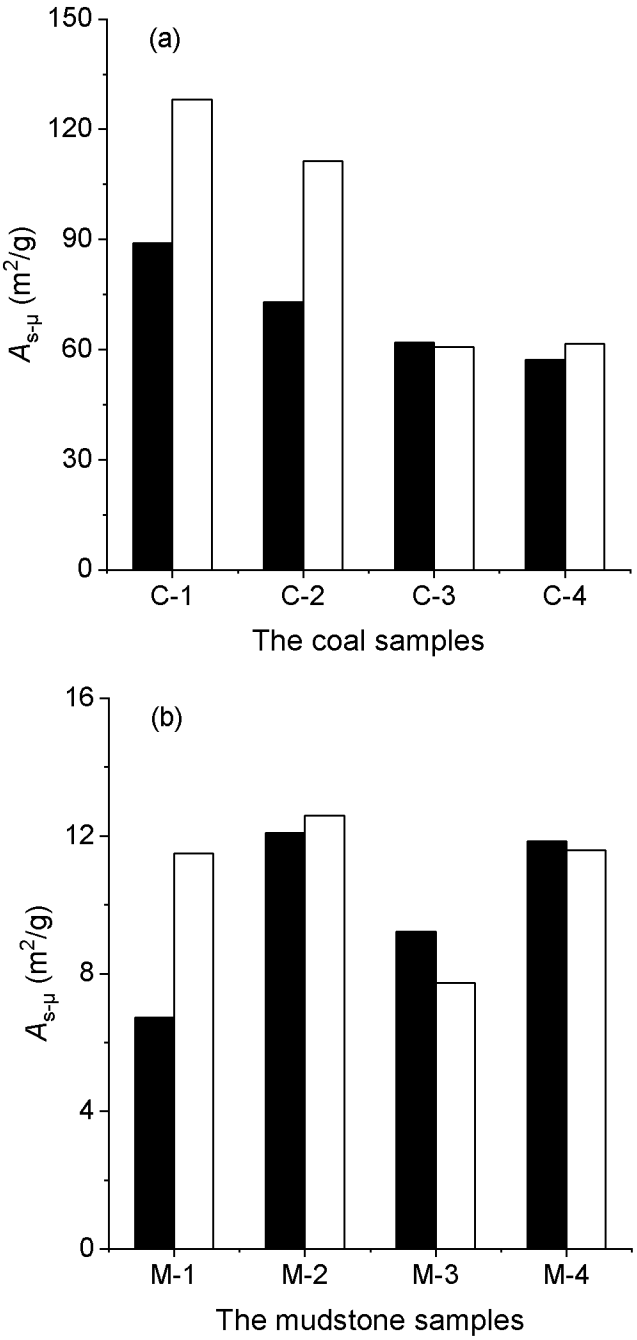

Figure 7 Specific surface areas of the a) coal and b) mudstone samples. The black bars represent the original samples and the white bars represent the extracted samples

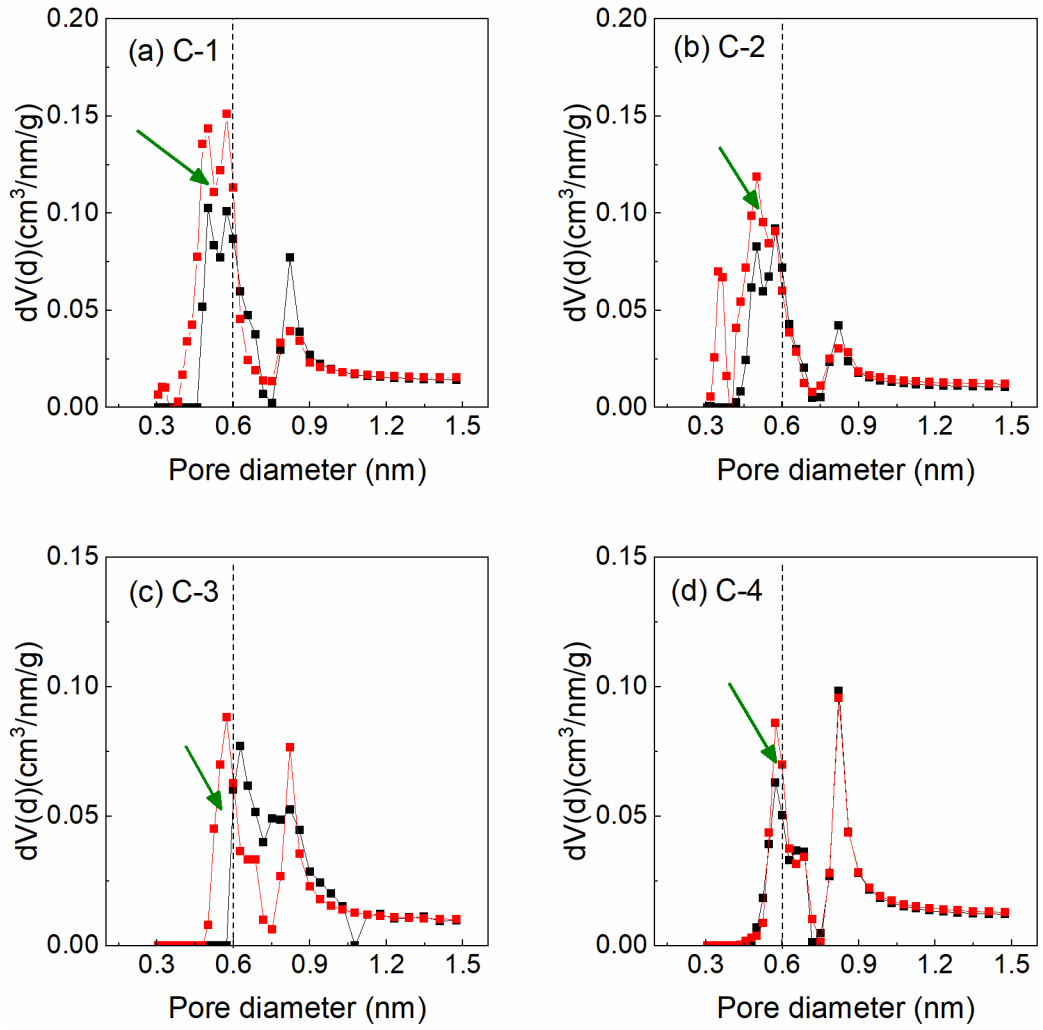

Figure 8 Micropore size distribution curves (CO_2 adsorption) of the coal samples. Black symbols and lines represent the original coals, and red symbols and lines, the extracted coals. The green arrows mark the increase of pores <0.6 nm. [print in colour]

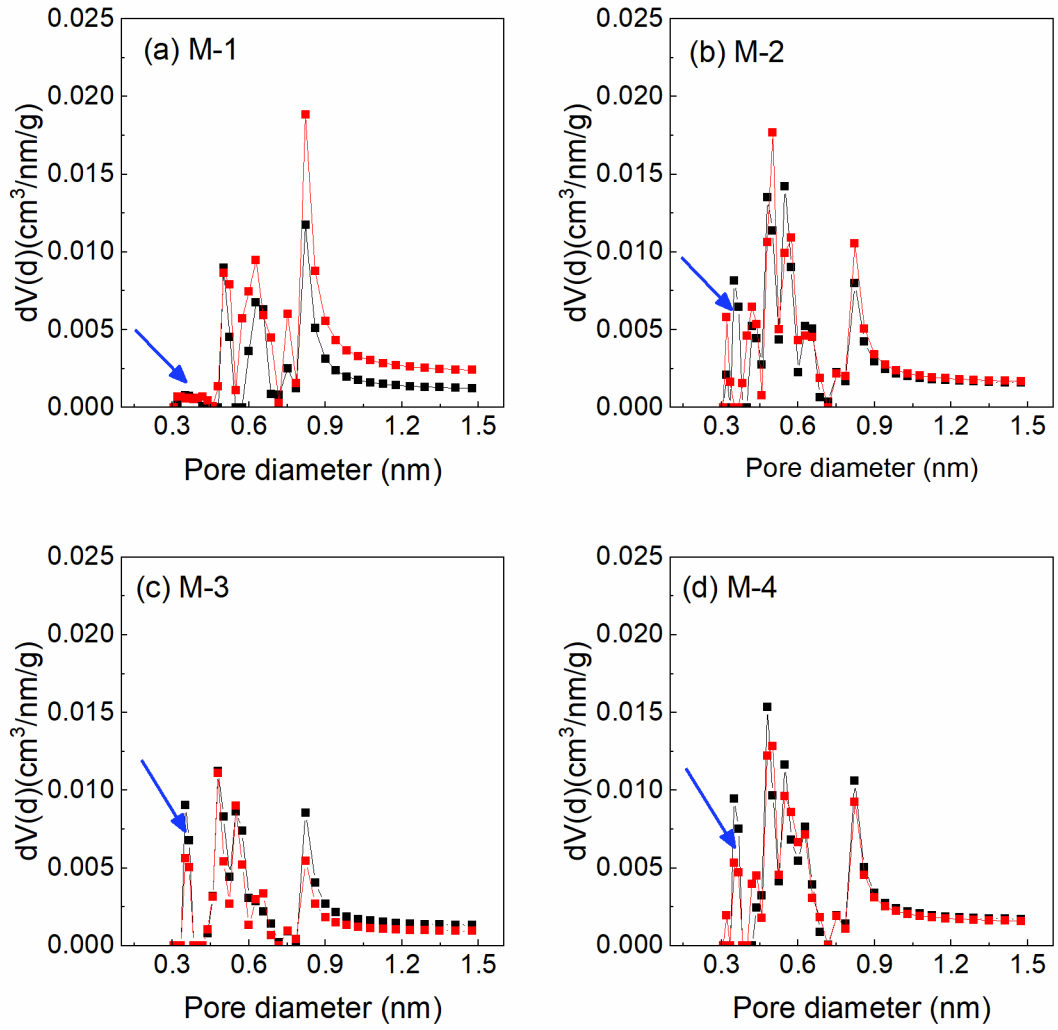

Figure 9 Micropore size distribution curves (CO_2 adsorption) of the mudstone samples. Black symbols and lines represents the original mudstones, and red symbols and lines, the extracted mudstones. The blue arrows mark the decrease of pores ~ 0.4 nm. [print in colour]

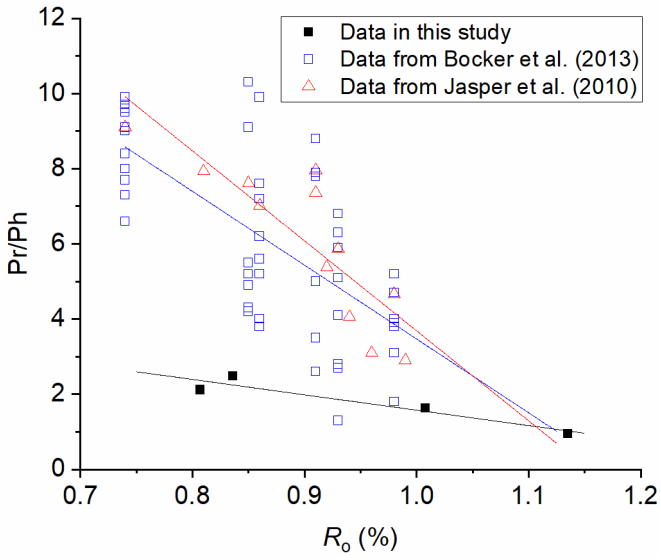

Figure 10 Plot of Pr/Ph vs R_o of the coal samples and some referenced data. [print in colour]

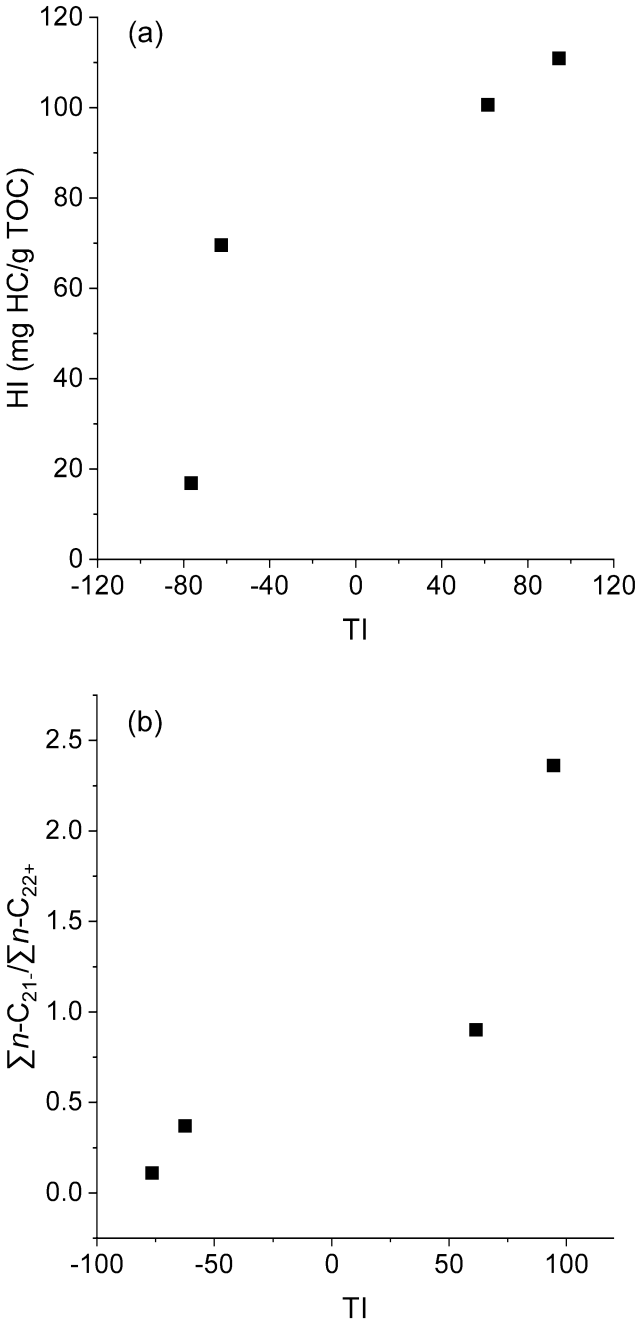

Figure 11 Relationships between (a) HI values and kerogen's Type Index, (b) $\sum n$-$C_{21-}/\sum n$-C_{22+} values and kerogen's Type Index.

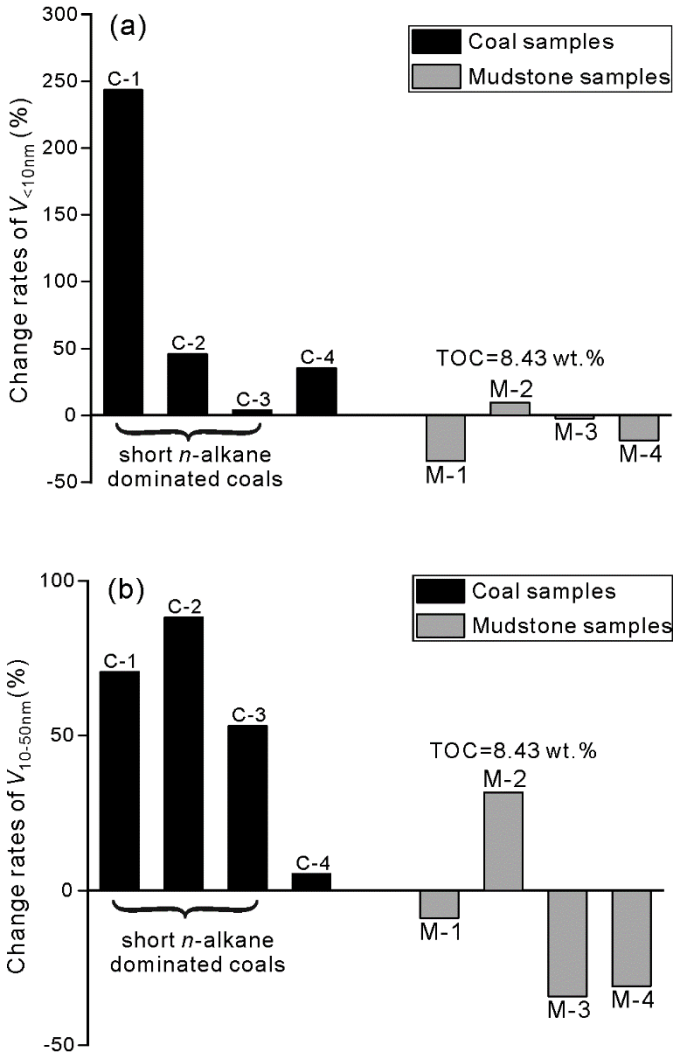

Figure 12 Change rates of (a) $V_{<10\ nm}$ and (b) $V_{10\text{-}50\ nm}$ of the coals (black bars) and the mudstones (gray bars).